Nonlinear light diffraction by electromagnetically induced gratings with $\mathcal{PT}$ symmetry in a Rydberg atomic gas

Chao Hang,[1,3,5,*] Weibin Li,[2,4] and Guoxiang Huang[1,3,5]

[1]*State Key Laboratory of Precision Spectroscopy, School of Physical and Material Sciences, East China Normal University, Shanghai 200062, China*

[2]*School of Physics and Astronomy, University of Nottingham, Nottingham NG7 2RD, United Kingdom*

[3]*NYU-ECNU Institute of Physics at NYU-Shanghai, Shanghai 200062, China*

[4]*Centre for the Mathematics and Theoretical Physics of Quantum Non-equilibrium Systems, University of Nottingham, Nottingham NG7 2RD, United Kingdom*

[5]*Collaborative Innovation Center of Extreme Optics, Shanxi University, Taiyuan, Shanxi 030006, China*

(Received 30 March 2019; published 8 October 2019)

Understanding and manipulating the non-Hermitian optical property based on coherent atomic gases is of great importance and has attracted much theoretical and experimental attentions. Advancing this study to the nonlinear optics regime is highly desirable due to its importance in fundamental physics and potential applications. In this work, we propose to realize a tunable electromagnetically induced grating (EIG) with parity-time ($\mathcal{PT}$) symmetry in a cold gas of Rydberg atoms, where interatomic interactions between Rydberg states are mapped to strong and long-range optical interactions, and investigate nonlinear light diffractions in this system. We show that for far-field diffraction, laser beams incident upon the $\mathcal{PT}$-symmetric EIG display distinctive asymmetric diffraction fringes, which can be actively manipulated through tuning the gain-absorption coefficient of the EIG, the incident intensity of the laser beam, and the nonlocality provided by Rydberg atoms. For near-field diffraction, the nonlinear Talbot diffraction carpets emerge and can be modulated by $\mathcal{PT}$ symmetry in the presence of strong nonlocal interactions, allowing the realization of controllable optical self-imaging. The results are not only imperative for the study of non-Hermitian nonlinear optics but also useful for characterizing the interatomic interaction in Rydberg gases and for designing new optical devices useful in optical information processing and transmission.

DOI: 10.1103/PhysRevA.100.043807

I. INTRODUCTION

In the past decades, the study of light diffraction in optical media whose refractive indices can be engineered has attracted enormous attention due to its significant applications in optical science and technology [1,2]. Among many systems, cold gases of trapped atoms have been utilized extensively, as their optical properties can be tuned through light-atom coupling. One paradigm is the creation of electromagnetically induced gratings (EIGs) by coupling atoms with spatially modulating laser lights in the form of standing waves [3–14]. Propagation of light fields in solid gratings leads to nontrivial diffraction, such as diffraction with perfect transmittance and focusing abilities [15,16] and the Talbot effect [17,18], which is known as a lensless self-imaging phenomenon. In particular, the Talbot effect has been experimentally observed recently with EIGs created in atomic gases [19]. On the other hand, there has been growing interest in the exploration of EIG-related optical phenomena in nonlinear regime. In the presence of relatively weak optical Kerr nonlinearity, the formation of vector dipole solitons [20] and photonic topological insulators [21] has been predicted with EIGs.

More importantly, through laser coupling of multilevel atoms, the optical refractive index with gain and absorption can be realized and tuned simultaneously, giving rise to optical media with parity-time ($\mathcal{PT}$) symmetry [22–27]. This makes it possible to simulate non-Hermitian quantum mechanics [28–31] in the optical domain [32]. In addition to fundamental interest, the exploration of optical $\mathcal{PT}$ symmetry has facilitated various applications, including nonreciprocal light propagation and unidirectional invisibility [33–35], coherent perfect absorbers [36–38], giant light amplification [39], single-mode lasers [40,41], supersensitive sensors [42,43], and so on [44]. The combined effects of $\mathcal{PT}$ symmetry and optical gratings in the linear optics regime lead to many interesting phenomena, such as beam rectification and dynamic localization [45], spatially asymmetric light diffraction [46–49], and a new class of self-imaging Talbot effects [50].

Optical nonlinearities in atomic gases are typically too weak for single photons and local. To go beyond the weak, local Kerr nonlinearity regime, electronically high-lying (Rydberg) states have recently been exploited to enhance interatomic interactions [51] through electromagnetically induced transparency (EIT). Lifetime in Rydberg states is proportional to n^3 (n is the principal quantum number), which is typically tens of microseconds. Most importantly, the van der Waals interactions between Rydberg atoms $\sim n^{11}$. The mapping of interatomic interactions to light fields generates strong and

*chang@phy.ecnu.edu.cn

long-range optical nonlinearities, which opens a new avenue of research on nonlocal nonlinear optics [52–56] and quantum nonlinear optics [57,58] and facilitates applications in quantum information processing [59–61]. Using Rydberg gases, a cooperative nonlinear grating has also been proposed to identify photon statistics [62] and to create nonlocal optical solitons with $\mathcal{PT}$ symmetry [63]. Although there are rapid developments in nonlocal nonlinear optics with Rydberg atoms, how to create EIGs with $\mathcal{PT}$ symmetry and explore and find intriguing properties of nonlinear light diffractions in the presence of nonlocal Kerr nonlinearity is still an open question.

In this work, we investigate nonlinear light diffractions from EIGs with $\mathcal{PT}$ symmetry and strong, long-range optical interactions in a cold gas of Rydberg atoms. Through a system with Rydberg-dressed EIT, an EIG with $\mathcal{PT}$ symmetry is built with additional ancillary laser fields, and at the same time, Rydberg interatomic interactions are mapped to the nonlocal Kerr nonlinearity of the probe light field. For a far-field diffraction, laser beams incident upon the $\mathcal{PT}$-symmetric EIG display drastic asymmetric diffraction fringes. We show that the diffraction asymmetry degree can be controlled by the gain-absorption coefficient of the EIG, the incident intensity of the laser beam, and the nonlocality provided by Rydberg atoms, which might be used to characterize the interatomic interaction property of the Rydberg gas. The active manipulation of intensities along different diffraction orders through laser parameters and nonlocal nonlinearity is also explored. For near-field diffraction, our investigation shows that the emerging Talbot effect from the $\mathcal{PT}$-symmetric EIG can be turned on and off by changing Rydberg interatomic interactions. Our study is useful for various applications in optical information processing and transmission, such as the design of novel optical beam dividers with desired intensities and the realization of controllable optical self-imaging.

The structure of the paper is as follows. In Sec. II, we describe the theoretical model under study and illustrate how to realize an EIG with $\mathcal{PT}$ symmetry in a Rydberg gas. In Sec. III, we investigate nonlinear Raman-Nath diffraction when a probe laser beam is normally incident upon a $\mathcal{PT}$-symmetric EIG with low and high incident intensities. In Sec. IV, we discuss nonlinear Talbot self-imaging and its active control in the system. Finally, in Sec. V we summarize the main results obtained in this work.

II. THEORETICAL MODEL AND PHYSICAL REALIZATION OF THE $\mathcal{PT}$-SYMMETRIC EIG

A. Model and basic equations

We start by considering a cold gas of a lifetime-broadened four-level atomic system (with atomic density $\mathcal{N}_a$) with the inverted-Y-type configuration suggested in [25] [see Fig. 1(a)]. The electric field acting with the atomic system reads $\mathbf{E} = \mathbf{E}_p + \mathbf{E}_c + \mathbf{E}_a$, with $\mathbf{E}_\alpha = \mathbf{e}_\alpha \mathcal{E}_\alpha \exp[i(\mathbf{k}_\alpha \cdot \mathbf{r} - \omega_\alpha t)] + \text{H.c.}$ ($\mathbf{e}_\alpha$ are unit polarization vectors, $\mathcal{E}_\alpha$ are field amplitudes). Here, a weak, spatially focused probe laser field $\mathbf{E}_p$ (with center wave number $k_p = \omega_p/c$ and angular frequency ω_p) couples the ground state $|1\rangle$ to the intermediate state $|3\rangle$; a strong control laser field $\mathbf{E}_c$ (with wave number $k_c = \omega_c/c$ and angular frequency ω_c) couples the low-lying state $|2\rangle$ and state $|3\rangle$. $\Delta_3 = \omega_p - (\omega_3 - \omega_1)$, $\Delta_2 = \omega_p - \omega_c - (\omega_2 - \omega_1)$, and $\Delta_4 = (\omega_4 - \omega_1) - \omega_p - \omega_a$ are, respectively, the one- and two-photon detunings; Γ_{13}, Γ_{23}, and Γ_{34} are, respectively, the spontaneous-emission decay rates from $|3\rangle$ to $|1\rangle$, $|3\rangle$ to $|2\rangle$, and $|4\rangle$ to $|3\rangle$. States $|1\rangle$, $|2\rangle$, and $|3\rangle$ and the probe and control fields constitute a standard Λ-type EIT configuration. The Λ-type EIT is, however, dressed by a high-lying Rydberg state $|4\rangle$ (with a large principal quantum number n), which is far off-resonantly (i.e., $\Delta_3 + \Delta_4 \gg \Omega_a$) coupled to $|3\rangle$ through an assistant laser field $\mathbf{E}_a$ (with wave number $k_a = \omega_a/c$ and angular frequency ω_a). Moreover, in order to realize an optical $\mathcal{PT}$ symmetry in such a Rydberg-dressed EIT system, an incoherent population pumping (at pumping rate Γ_{21}) is applied, coupled to the two low-lying states $|1\rangle$ and $|2\rangle$. In addition, the control and the assistant fields are assumed to be spatially modulated (see below).

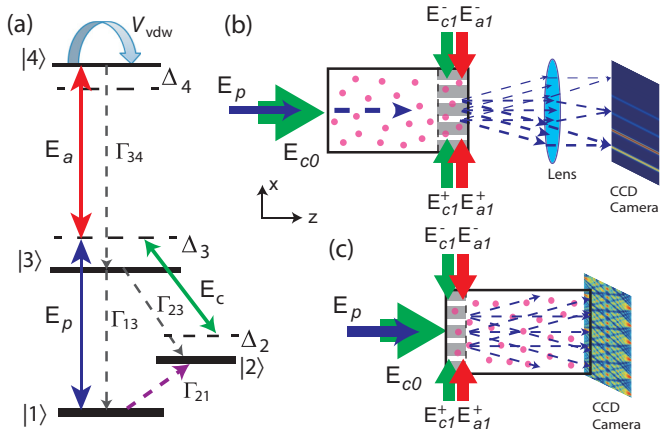

FIG. 1. (a) Level diagram and excitation scheme of the Rydberg-dressed EIT. States $|1\rangle$, $|2\rangle$, and $|3\rangle$ constitute a Λ-type EIT configuration, where the probe laser field E_p couples the transition $|1\rangle \leftrightarrow |3\rangle$ and the control laser field E_c couples the transition $|2\rangle \leftrightarrow |3\rangle$. Δ_j are detunings and Γ_{jl} are the spontaneous-emission decay rate from $|l\rangle$ to $|j\rangle$. The Λ-type EIT is dressed by a high-lying Rydberg state $|4\rangle$, which is far-off-resonantly coupled to state $|3\rangle$ through an assistant laser field E_a. An incoherent pumping (at pumping rate Γ_{21}) is used to pump atoms from $|1\rangle$ to $|2\rangle$. The interaction between Rydberg atoms is described by the van der Waals potential V_{vdw} (with its expression given in the text). (b, c) Possible setups of light diffractions for probe beams normally incident on $\mathcal{PT}$-symmetric EIGs. A cold Rydberg gas of ^{87}Rb atoms is filled in atomic cells, consisting of two parts in the z direction. E_{c0} and E_{a0} are homogeneous parts of the control and assistant fields. E_{c0} (E_{a0}) is incident to the atomic cells along the $+z$ ($-z$) direction (E_{a0} is not shown). Additional laser pairs $E_{c1}^{\pm}$ and $E_{a1}^{\pm}$ are applied along the x direction, introducing spatial modulations in the control and assistant laser fields and hence realizing $\mathcal{PT}$-symmetric EIGs in shaded parts of cells.

For relatively high atomic densities, the dynamics of the system is described by the spatially continuous Hamiltonian $\hat{H} = \mathcal{N}_a \int d^3\mathbf{r} \hat{\mathcal{H}}(\mathbf{r}, t)$, with the Hamiltonian density $\hat{\mathcal{H}}(\mathbf{r}, t) = \sum_{j=1}^{4} \hbar \Delta_j \hat{S}_{jj}(\mathbf{r}, t) - \hbar[\Omega_p \hat{S}_{13}(\mathbf{r}, t) + \Omega_a \hat{S}_{34}(\mathbf{r}, t) + \Omega_c \hat{S}_{23}(\mathbf{r}, t) + \text{H.c.}] + \mathcal{N}_a \int d^3\mathbf{r}' \hat{S}_{44}(\mathbf{r}', t) \hbar V(\mathbf{r}' - \mathbf{r}) \hat{S}_{44}(\mathbf{r}, t)$, where the electric-dipole and rotating-wave approximations have been applied. Here

$\hat{S}_{jl} = |l\rangle\langle j|\, e^{i[(\mathbf{k}_l-\mathbf{k}_j)\cdot\mathbf{r}-(\omega_l-\omega_j+\Delta_l-\Delta_j)t]}$ is the transition operator related to states $|j\rangle$ and $|l\rangle$, satisfying the commutation relation $[\hat{S}_{jl}(\mathbf{r},t), \hat{S}_{\mu\nu}(\mathbf{r}',t)] = (1/\mathcal{N}_a)\delta(\mathbf{r}-\mathbf{r}')[\delta_{j\nu}\hat{S}_{\mu l}(\mathbf{r}',t) - \delta_{\mu l}\hat{S}_{j\nu}(\mathbf{r}',t)]$, with $\hbar\omega_j$ the eigenenergy of level $|j\rangle$; $\Omega_p = (\mathbf{e}_p\cdot\mathbf{p}_{31})\mathcal{E}_p/\hbar$, $\Omega_c = (\mathbf{e}_c\cdot\mathbf{p}_{32})\mathcal{E}_c/\hbar$, and $\Omega_a = (\mathbf{e}_a\cdot\mathbf{p}_{43})\mathcal{E}_a/\hbar$ are, respectively, half Rabi frequencies of the probe, control, and assistant fields, with $\mathbf{p}_{ij}$ the electric dipole matrix elements associated with the transition $|i\rangle \leftrightarrow |j\rangle$. The latter term represents the contribution due to atom-atom interaction. The interaction between the Rydberg atom at position $\mathbf{r}$ and the one at position $\mathbf{r}'$ is described by the long-range potential $\hbar V_{\rm L}(\mathbf{r}'-\mathbf{r})$, with $V_{\rm L}(\mathbf{r}'-\mathbf{r}) = C_6/|\mathbf{r}'-\mathbf{r}|^6$ (C_6 is called dispersion coefficient).

The dynamical evolution of atoms is governed by the optical Bloch equation

$$\frac{\partial\rho}{\partial t} = -\frac{i}{\hbar}[\hat{H},\rho] - \Gamma[\rho], \tag{1}$$

where ρ is the density matrix, with matrix elements $\rho_{jl} \equiv \langle\hat{S}_{jl}\rangle$, and Γ is the relaxation matrix, contributed from the spontaneous emission and dephasing in the system. The explicit form of Eq. (1) is given in Appendix A. The wave equation of the probe field is described by the Maxwell equation, which, under the slowly varying amplitude approximation, reads

$$i\left(\frac{\partial}{\partial z}+\frac{1}{c}\frac{\partial}{\partial t}\right)\Omega_p + \frac{1}{2k_p}\left(\frac{\partial^2}{\partial x^2}+\frac{\partial^2}{\partial y^2}\right)\Omega_p + \frac{k_p}{2}\chi_p\,\Omega_p = 0, \tag{2}$$

with $\chi_p = \mathcal{N}_\alpha(\mathbf{e}_p\cdot\mathbf{p}_{13})^2\rho_{31}/(\varepsilon_0\hbar\Omega_p)$ the probe-field susceptibility. The term with second derivatives with respect to x and y describes the diffraction effect. The propagation directions of the laser fields are assumed to be $\mathbf{k}_p = (0,0,k_p)$, $\mathbf{k}_c = (0,0,k_c)$, and $\mathbf{k}_a = (0,0,-k_a)$ for suppressing the first-order Doppler effect. We are interested in the stationary state, in which the probe, control, and assistant fields have very long durations so that the time derivatives in the Bloch and Maxwell equations can be neglected.

Since the probe field is much weaker than the other two fields, perturbation expansions of Ω_p and ρ_{jl} ($j,l = 1$–4) can be employed to solve the Bloch equation, (1) [64,65]. With the solution of ρ_{31} exact to the third order of Ω_p, the optical susceptibility of the probe field can be expressed as $\chi_p = \chi_p^{(1)} + \chi_{p,1}^{(3)}|\mathcal{E}_p|^2 + \int d^3\mathbf{r}'\chi_{p,2}^{(3)}(\mathbf{r}'-\mathbf{r})|\mathcal{E}_p(\mathbf{r}')|^2$, where $\chi_p^{(1)}$ is the linear optical susceptibility and $\chi_{p,1}^{(3)}$ [$\chi_{p,2}^{(3)}$] is the local [nonlocal] nonlinear optical susceptibility, contributed by the atom-photon [atom-atom] interaction. The expressions for $\chi_p^{(1)}$, $\chi_{p,1}^{(3)}$, and $\chi_{p,2}^{(3)}$ read

$$\chi_p^{(1)} = \frac{\mathcal{N}_\alpha(\mathbf{e}_p\cdot\mathbf{p}_{13})^2}{\varepsilon_0\hbar}\alpha_{31}^{(1)}, \tag{3a}$$

$$\chi_{p,1}^{(3)} = \frac{\mathcal{N}_\alpha(\mathbf{e}_p\cdot\mathbf{p}_{13})^4}{\varepsilon_0\hbar^3 D}\left[d_{21}d_{41}\left(\alpha_{33}^{(2)}-\alpha_{11}^{(2)}\right) - \Omega_a d_{41}\alpha_{23}^{(2)} - \Omega_c^* d_{21}\alpha_{43}^{(2)}\right], \tag{3b}$$

$$\chi_{p,2}^{(3)} = \frac{\mathcal{N}_\alpha^2(\mathbf{e}_p\cdot\mathbf{p}_{13})^4}{\varepsilon_0\hbar^3}V_{\rm L}(\mathbf{r}'-\mathbf{r})\alpha_{41}^{(1)*}\alpha_{4141}^{(2)}, \tag{3c}$$

respectively, with $D = d_{32}d_{42}d_{43} - |\Omega_c|^2 d_{32} - |\Omega_a|^2 d_{43}$ and $d_{jl} = \Delta_j - \Delta_l + i\gamma_{jl}$. Here $\gamma_{ij} = (\Gamma_i+\Gamma_j)/2 + \gamma_{ij}^{\rm col}$ and $\Gamma_j = \sum_{i<j}\Gamma_{ij}$, with Γ_{ij} the spontaneous emission decay rate and $\gamma_{ij}^{\rm col}$ the dephasing rate from $|j\rangle$ to $|i\rangle$. Expressions for $\alpha_{ij}^{(m)}$ ($m = 1, 2$) and $\alpha_{4141}^{(2)}$ are presented in Appendix A. It is noteworthy that both $\chi_p^{(1)}$ and $\chi_{p,1}^{(3)}$ are proportional to $\mathcal{N}_a$, whereas $\chi_{p,2}^{(3)}$ is proportional to $\mathcal{N}_a^2$. On the other hand, $\chi_{p,1}^{(3)}$ becomes 0 under the exact EIT condition ($\Delta_2 = 0$), however, $\chi_{p,2}^{(3)}$ is nonzero under the exact EIT condition.

For simplicity, we assume that the spatial extension of the input probe beam along the y and z directions is much larger than that of the atom-atom interaction, so the behavior of the third-order nonlocal nonlinear optical susceptibility in the y and z directions can be taken as a local one. Bearing this in mind and substituting the derived χ_p into the Maxwell equation, (2), we obtain the dimensionless nonlocal nonlinear Schrödinger equation

$$i\frac{\partial U}{\partial\zeta} = -\frac{\partial^2 U}{\partial\xi^2} + V(\xi)U + \int d\xi' W_2(\xi'-\xi)|U(\xi',\zeta)|^2 U(\xi,\zeta), \tag{4}$$

where $U = \Omega_p/\Omega_{p0}$ (Ω_{p0} is the scaled input Rabi frequency of the probe beam), $\zeta = z/L_{\rm diff}$ ($L_{\rm diff} \equiv 2k_p w_0^2$ is the characteristic diffraction length, with w_0 the width of the probe beam), and $(\xi,\xi') = (x,x')/w_0$. The dimensionless linear potential is defined by $V(\xi) = -k_p^2 w_0^2\chi_p^{(1)}(\xi)$; the nonlinear response function (i.e., the integral kernel) is given by $W_2(\xi'-\xi) = -2k_p^3 w_0^6\Omega_{p0}^2\iint d\eta d\zeta\,\chi_{p,2}^{(3)}(\xi'-\xi,\eta,\zeta)$, with $\eta = y/w_0$. Note that in Eq. (4) we have neglected the term of the local Kerr nonlinearity $W_1|U|^2U$ ($W_1 \equiv -k_p^2 w_0^2\Omega_{p0}^2\chi_{p,1}^{(3)}$), which is usually much smaller than the term standing for the nonlocal Kerr nonlinearity [56].

B. Physical realization of $\mathcal{PT}$-symmetric EIGs

The analytical result applies to the Rydberg EIT with cold alkali atoms in general. To be concrete, we consider laser-cooled ^{87}Rb atoms as an example, where the atomic levels are assigned as $|1\rangle = |5S_{1/2}, F=1\rangle$, $|2\rangle = |5S_{1/2}, F=2\rangle$, $|3\rangle = |5P_{3/2}, F=3\rangle$, and $|4\rangle = |nS_{1/2}\rangle$. The incoherent pumping rate and the spontaneous decay rates are $\Gamma_{21} \approx 2\pi\times 0.1$ MHz, $\Gamma_3 \approx 2\pi\times 6$ MHz, and $\Gamma_4 \approx 2\pi\times 3$ kHz, respectively. The dispersion parameter $C_6 \approx 2\pi\times 140$ GHz μm^6 for $n = 60$. The density of the atomic gas is chosen as $\mathcal{N}_a = 1.0\times 10^{12}$ cm^{-3}. The detunings in the system are $\Delta_2 = -2.74$ MHz, $\Delta_3 = 50$ MHz, and $\Delta_4 = 100$ MHz, respectively. The Rabi frequencies of the control and assistant fields are both of the order of 10 MHz, and hence $(\Delta_3+\Delta_4)/\Omega_a \sim 10 \gg 1$, i.e., the system works in the Rydberg-dressed EIT regime [63].

The target potential we seek is a $\mathcal{PT}$-symmetric periodic function with the form

$$V(\xi) = V_0 + V_1\sin^2(\xi) + iV_2\sin(2\xi), \tag{5}$$

where V_0 contributes a constant phase, and V_1 and V_2 ($|V_1|$ and $|V_2| \ll V_0$) characterize, respectively, the amplitudes of the real and imaginary parts of the target potential. Using the method proposed in [22,26], with parameter values from ^{87}Rb atoms, the target potential can be created by the spatially

modulated control and assistant fields (more details are given in Appendix B), given by

$$\Omega_c(\xi)/\Omega_{c0} \approx 1 + 0.21V_2 \sin(2\xi), \tag{6a}$$

$$\Omega_a(\xi)/\Omega_{a0} \approx 1 - 1.67V_1 \sin^2\xi - 5.74V_2 \sin(2\xi), \tag{6b}$$

with $V_0 = -27.67$, $\Omega_{c0} = 1.5 \times 10^7\ \mathrm{s}^{-1}$, and $\Omega_{a0} = 1.0 \times 10^7\ \mathrm{s}^{-1}$. Here we remark that expressions (6a) and (6b) ensure the $\mathcal{PT}$ symmetry only in the finite range of ξ ($\equiv x/w_0$), while for large ξ significant deviations may occur.

From Eqs. (5) and (6), the real and imaginary parts of the potential are determined simultaneously by the spatial modulations in the control and assistant fields, which can be generated experimentally by the interference of additional pairs of laser fields [19,24]. In Figs. 1(b) and 1(c), E_{c0} and E_{a0} are homogeneous parts of the control and assistant fields. E_{c0} is assumed to be incident to the atomic cells in the $+z$ direction, while E_{a0} is incident to the atomic cells along the $-z$ direction (not shown). Additional laser pairs, $E_{c1}^{\pm}$ and $E_{a1}^{\pm}$, along the x direction introduce, respectively, spatial modulations in the control and assistant fields for realizing $\mathcal{PT}$-symmetric EIGs. Note that $\mathcal{PT}$-symmetric EIGs are built only in small parts of atomic cells [denoted by shaded regions in Figs. 1(b) and 1(c)].

Turning to the nonlocal Kerr nonlinearity, with the parameters of ^{87}Rb atoms and $\Omega_{p0} \approx 3.0 \times 10^6\ \mathrm{s}^{-1}$ we obtain the expression

$$W_2(\xi' - \xi) \approx 0.02 \iint d\eta d\zeta \left\{ 1 + i0.14 + \frac{\left[(\xi' - \xi)^2 + \eta^2 + 4k_p^2 w_0^2 \zeta^2\right]^3}{(0.45R_b/w_0)^6} \right\}^{-1}, \tag{7}$$

where $R_b \approx 9.1\ \mu$m is the radius of the Rydberg blockade [66]. Moreover, the response function W_2 obeys the normalization condition $\int d\xi W_2(\xi' - \xi) \approx 1$, which is consistent with the limit $W_2(\xi' - \xi) = \delta(|\xi' - \xi|)$. Since W_2 is positive, the nonlocal Kerr nonlinearity in Eq. (4) is self-defocusing due to the repulsive atom-atom interaction considered here. It is also possible to have a nonlocal self-focusing Kerr nonlinearity by using attractive interatomic interactions, e.g., by considering ^{88}Sr atoms [56].

To characterize the nonlocal optical property, we define the nonlocality degree of the Kerr nonlinearity of the system, which is the ratio between R_b and w_0, i.e.,

$$\sigma \equiv R_b/w_0. \tag{8}$$

When $w_0 \gg R_b$, one has $\sigma \approx 0$, in which case the nonlocal nonlinear potential becomes a local one and hence Eq. (4) is reduced to a local NLSE.

Figure 2(a) shows the real and imaginary parts of the linear potential, i.e., $\mathrm{Re}(V - V_0)$ (solid black line) and $\mathrm{Im}(V - V_0)$ (dashed red line), as functions of ξ. Rabi frequencies of the control and assistant fields, i.e., $\Omega_c(\xi)/\Omega_{c0}$ (solid black line) and $\Omega_c(\xi)/\Omega_{c0}$ (dashed red line), as functions of ξ are also illustrated. Figure 2(b) shows the spatial distributions of the real and imaginary parts of the nonlocal nonlinear response function W_2 in Eq. (4), i.e., $\mathrm{Re}(W_2)$ (solid black line) and $\mathrm{Im}(W_2)$ (dotted red line), as functions of ξ with $w_0 = R_b$ and $\sigma = 0.45$. It is noteworthy that the maximum

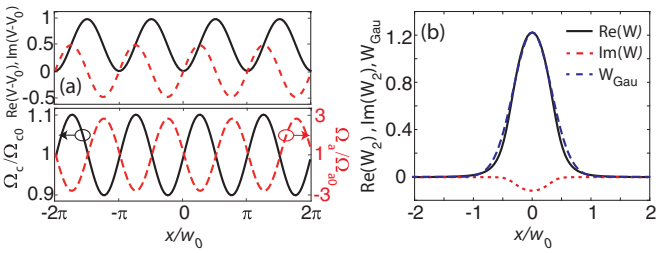

FIG. 2. (a) Upper panel: Real and imaginary parts of the linear potential, i.e., $\mathrm{Re}(V - V_0)$ (solid black line) and $\mathrm{Im}(V - V_0)$ (dashed red line), as functions of x/w_0. Lower panel: Rabi frequencies of the control and assistant fields, i.e., Ω_c/Ω_{c0} (solid black line) and Ω_a/Ω_{a0} (dashed red line), as functions of x/w_0. Here the amplitude of the real (imaginary) part of the linear potential $V_1 = 1$ ($V_2 = 0.5$). (b) Spatial distributions of the real and imaginary parts of the nonlinear response function W_2 in Eq. (4) (for repulsive atom-atom interaction), i.e., $\mathrm{Re}(W_2)$ (solid black line) and $\mathrm{Im}(W_2)$ (dotted red line), as functions of x/w_0 with $w_0 = R_b$ ($\sigma = 1$). The dashed blue line is the plot of the function $W_{\mathrm{Gau}} = e^{-(\xi/0.45)^2}/(0.45\sqrt{\pi})$.

of $-\mathrm{Im}(W_2)$ is approximately one order of magnitude smaller than that of $\mathrm{Re}(W_2)$. To a large extent, W_2 can be approximated by its real part, namely, $W_2 \approx \mathrm{Re}(W_2)$. Additionally, $\mathrm{Re}(W_2)$ can be approximated by a Gaussian function, i.e., $W_{\mathrm{Gau}} = e^{-(\xi/0.45)^2}/(0.45\sqrt{\pi})$, which is also illustrated in Fig. 2(b) by the dashed blue line.

III. RAMAN-NATH DIFFRACTION BY $\mathcal{PT}$-SYMMETRIC EIGs

A. General result for Raman-Nath diffraction

When the probe beam is normally incident to a $\mathcal{PT}$-symmetric EIG and is wide enough to cover several or more spatial periods of the EIG, a far-field diffraction of the probe beam may occur. It is noteworthy that plane diffraction gratings operate in two diffraction regimes: the Bragg regime (or thick grating) and the Raman-Nath regime (or thin grating). Here we focus on the far-field light diffraction in the Raman-Nath regime, where multiple diffraction waves are generated. As a possible setup for observing such light diffraction, we assume that a cold Rydberg gas of ^{87}Rb atoms is filled in an atomic cell, consisting of two parts in the z direction, as shown in Fig. 1(b). The spatial modulations in the control and assistant fields are introduced only in the right part of the atomic cell and hence realize the $\mathcal{PT}$-symmetric EIG in that part. In addition, the length of the region without EIG (the left part) is L and the length of the region with EIG (the right part) is d, obeying the condition $d \ll L \ll L_{\mathrm{diff}}$. Then the probe field experiences an enhanced nonlinearity during its propagation in the long region without EIG (the left part) and undergoes diffraction in the short region with EIG (the right part).

The transmission function $T(\xi)$ of the probe field is defined by the ratio of the output field amplitude to the input field amplitude, which can be obtained by solving Eq. (4) in the absence of the diffraction term because $d \ll L < L_{\mathrm{diff}}$. It is easy to obtain that

$$T(\xi) = e^{-iV_0(L+d)+[V_2\sin(2\xi)-iV_1\sin^2(\xi)]d} \times e^{-i\int_0^{L+d} d\zeta \int_{-\infty}^{\infty} d\xi' W_2(\xi'-\xi)|U(\xi',\zeta)|^2}. \tag{9}$$

In contrast with previous studies [47–49], the transmission function, (9), depends not only on the linear potential but also on the nonlocal nonlinear potential and the intensity of the probe field.

The diffraction spectrum of the weak probe field is obtained by the Fourier transform of $T(\xi)$. The diffraction intensity function can be written as [3]

$$I_p(\theta) = |F(\theta)|^2 \frac{\sin^2(N\pi\Lambda\sin\theta/\lambda_p)}{N^2\sin^2(\pi\Lambda\sin\theta/\lambda_p)}, \tag{10}$$

where θ denotes the diffraction angle of the probe beam with respect to the z direction, N represents the number of spatial periods of the grating illuminated by the probe beam in the x direction, Λ is the period of the grating along the x direction, and $F(\theta)$ is the Fraunhofer diffraction of a single space period Λ given by

$$F(\theta) = \frac{1}{\tau}\int_0^\tau d\xi T(\xi) e^{-i2\pi w_0 \xi \sin\theta/\lambda_p}, \tag{11}$$

with $\tau = \Lambda/w_0$ and $\lambda_p = 2\pi c/\omega_p$ the center wavelength of the probe beam. When the condition $\sin\theta_m = m\lambda_p/\Lambda$ ($m = 0, \pm1, \pm2, \ldots$) is satisfied, we obtain the probe-beam intensity I_p^m along the mth-order diffraction direction, given by

$$I_p^m = |F(\theta_m)|^2 = \left|\frac{1}{\tau}\int_0^\tau d\xi T(\xi) e^{-i2\pi m\xi/\tau}\right|^2. \tag{12}$$

B. Raman-Nath diffraction in the linear regime

We first discuss the Raman-Nath diffraction for the case of a small probe-beam power. For convenience in the following discussion, we adopt the parameters of Rb^{87} atoms and set $L = 1$ cm and $d = 10\ \mu$m. Additionally, we take $w_0 = 2.5\pi R_b \approx 71\ \mu$m, which leads to $L_{\rm diff} \approx 7.9$ cm and hence $d/L_{\rm diff} \sim 10^{-3} \ll 1$. A single space period of the EIG is chosen as $\Lambda = \pi R_b \approx 28\ \mu$m and hence the number of illuminated spatial periods is $N = 2w_0/\Lambda = 5$.

To investigate the influence of the gain-absorption coefficient of the $\mathcal{PT}$-symmetric EIG on light diffraction, we fix $V_1 = 4$ and $\sigma = 0$ (i.e., without the long-range interactions), and increase V_2 from 0. We assume that the input beam has a Gaussian distribution $U_{\rm in}(x) \equiv U(x, z = 0) = U_0\, e^{-x^2/(2w_0^2)}$, where the amplitude $U_0 = 0.09$. The light power of the input probe beam is small, i.e., $P \equiv \int_{-\infty}^{\infty} dx|U_{\rm in}(x)|^2 \approx 1$. Since the incident intensity of the probe beam is much less than 1, the nonlinear effect of the system induced by the probe beam is not important and the light diffraction is mainly a linear one.

Figures 3(a) and 3(b) show the diffraction intensity $I_p(\theta)$ [defined by Eq. (10)] as a function of $\sin\theta$ and z/d for $V_2 = 0$ and $V_2 = 2$ (the spontaneous $\mathcal{PT}$-symmetry-breaking point of the grating), respectively. The corresponding diffraction intensity distribution at the position $z = d$ is shown in Fig. 3(c). We see that when $V_2 = 0$ (the grating is real), the diffraction intensity distribution is symmetric in the x direction. However, when $V_2 > 0$ (the grating is complex), the diffraction intensity distribution becomes asymmetric in the x direction. Moreover, the power of the probe beam increases rapidly at $V_2 = 2$ because the EIG transforms from the unbroken $\mathcal{PT}$ phase (UPTP) to the broken $\mathcal{PT}$ phase (BPTP).

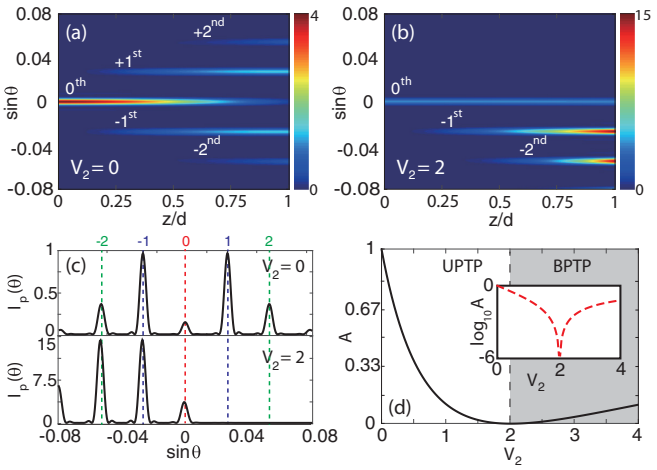

FIG. 3. Linear Raman-Nath diffraction fringes in the Rydberg gas for different gain-absorption coefficients of the $\mathcal{PT}$-symmetric EIG by taking $V_1 = 4$, $\sigma = 0$, and $P = 1$ (i.e., small probe-beam power). The input condition is given in the text. (a, b) Diffraction intensities, $I_p(\theta)$, as functions of $\sin\theta$ and z/d (d is the thickness of the grating), respectively, for $V_2 = 0$ [i.e., (a), where 0th-order, $\pm$1st-order, and $\pm$2nd-order diffraction fringes are shown] and for $V_2 = 2$ [i.e., (b), where 0th-order, $-$1st-order, and $-$2nd-order diffraction fringes are shown], respectively. (c) Corresponding diffraction intensity distributions at $z = d$. (d) Symmetry degree of the diffraction, A, as a function of V_2. The white region denotes the unbroken $\mathcal{PT}$ phase (UPTP), while the shaded region denotes the broken $\mathcal{PT}$ phase (BPTP). $A_{\rm min} \sim 10^{-6}$, obtained at $V_2(A_{\rm min}) = 2$. Inset: $\log_{10} A$ as a function of V_2.

The asymmetry of the diffraction intensity distribution for nonzero V_2 is a result of the out-of-phase interplay of amplitude and phase modulations of transmission function. In order to present the asymmetry degree of the diffraction intensity distribution, we define the symmetry degree

$$A \equiv I_p^{(1)}/I_p^{(-1)}, \tag{13}$$

which is the ratio between the intensity of the first-order diffraction intensity distribution (the $+$1st-order fringe) and that of the $-$1st-order diffraction intensity distribution (the $-$1st-order fringe). Then the asymmetry degree is determined by $1 - A$, i.e., the larger $1 - A$, the more asymmetric the diffraction intensity distribution. Clearly, the diffraction pattern becomes asymmetric if $A \neq 1$. Figure 3(d) shows A as a function of V_2. We see that A decreases from 1 to nearly 0 as V_2 increases from 0 to 2 and then increases slightly as V_2 increases from 2 to 4. In the inset, we show $\log_{10} A$ as a function of V_2. The minimum of A is of the order of 10^{-6}, i.e., $A_{\rm min} \sim 10^{-6}$, which is obtained at $V_2(A_{\rm min}) = 2$.

To understand the fact that $A_{\rm min}$ is obtained when V_2 is taken as the $\mathcal{PT}$-symmetry-breaking point, we rewrite the optical potential in Eq. (5) as $V(\xi) = V_0 + V_1 - (V_1/4)[(1 - q)e^{i2\xi} + (1 + q)e^{-i2\xi}]$, where $q = 2V_2/V_1$. Obviously, $V(\xi)$ has two components, $e^{i2\xi}$ and $e^{-i2\xi}$, representing moving gratings towards the positive and negative directions in the x coordinate. When $q = 0$ (i.e., $V_2 = 0$), moving gratings towards the positive and negative directions have the same amplitudes, resulting in a symmetric diffraction [Fig. 3(a)]. However,

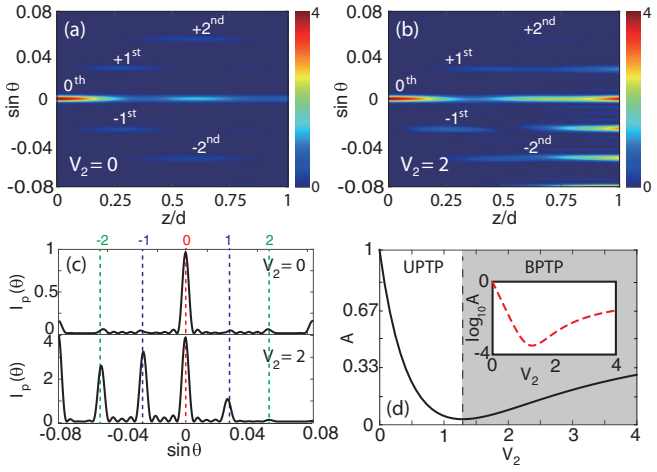

FIG. 4. Nonlinear Raman-Nath diffraction fringes in the Rydberg gas for different gain-absorption coefficients of the $\mathcal{PT}$-symmetric EIG by taking $V_1 = 4$, $\sigma = 0$, and $P = 100$ (i.e., large probe-beam power). (a, b) Diffraction intensities $I_p(\theta)$ as functions of $\sin\theta$ and z/d for $V_2 = 0$ [(a), where 0th-order, $\pm$1st-order, and $\pm$2nd-order diffraction fringes are shown] and for $V_2 = 2$ [(b), where 0th-order, -1st-order, and -2nd-order diffraction fringes are shown], respectively. (c) Corresponding diffraction intensity distributions at $z = d$. (d) Symmetry degree of the diffraction, A, as a function of V_2. The white (shaded) region denotes the UPTP (BPTP). $A_{\min} \sim 10^{-3}$, obtained at $V_2(A_{\min}) \approx 1.3$. Inset: $\log_{10} A$ as a function of V_2.

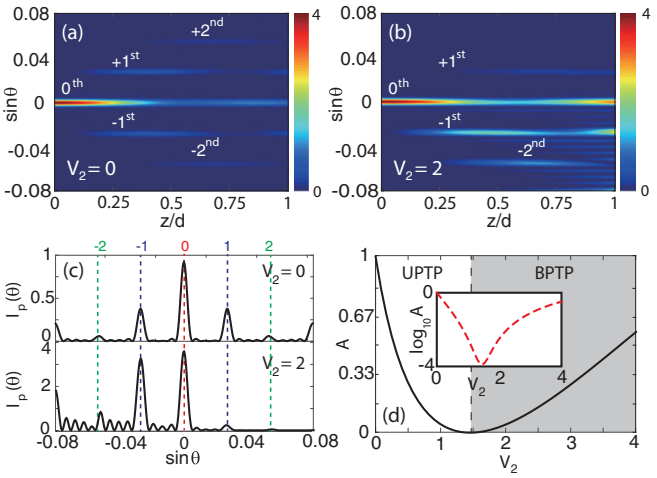

FIG. 5. Nonlinear Raman-Nath diffraction fringes in the Rydberg gas for a large nonlocality degree of the Kerr nonlinearity ($\sigma = 10$) by taking $V_1 = 4$ and $P = 100$. (a, b) Diffraction intensities $I_p(\theta)$ as functions of $\sin\theta$ and z/d for $V_2 = 0$ and $V_2 = 2$, respectively. (c) Corresponding diffraction intensity distributions at $z = d$. (d) Symmetry degree of the diffraction, A, as a function of V_2. The white (shaded) region denotes the UPTP (BPTP). $A_{\min} \sim 10^{-4}$, obtained at $V_2(A_{\min}) \approx 1.5$. Inset: $\log_{10} A$ as a function of V_2.

when $q \neq 0$ ($V_2 \neq 0$) the moving gratings towards the positive and negative directions have different amplitudes, resulting in the asymmetric diffraction pattern [Fig. 3(b)]. When $q = 1$ (i.e., $V_2 = 2$, corresponding to the $\mathcal{PT}$-symmetry-breaking point), there is only one moving grating towards the negative direction, and hence the most asymmetric diffraction pattern appears.

C. Raman-Nath diffraction in the nonlinear regime

Because of the strong atom-atom interaction in the Rydberg gas, which brings a significant nonlinear effect to the light propagation, the diffraction of the probe beam will become highly nonlinear when its incident intensity is increased. To illustrate this point, we focus here on the case with $U_0 = 0.9$ (and hence $P \approx 100$, which corresponds to a diffraction with a large probe-beam power), with the numerical result shown in Fig. 4.

In the figure, we see that for both $V_2 = 0$ [Fig. 4(a)] and $V_2 = 2$ [Fig. 4(b)] the intensity for the zeroth-order diffraction fringe is greatly enhanced. However, intensities for the high-order diffraction fringes are largely suppressed, which can be seen clearly in Figs. 4(a)–4(c). Moreover, in this large-power diffraction case $A_{\min} \approx 10^{-3}$, which is much larger than in the above case of linear diffraction. This implies that the domain of the UPTP is significantly reduced [see Fig. 4(d)].

The physical reason behind the result obtained in Fig. 4 is that the linear and nonlinear potentials in Eq. (4) reduce to an effective optical potential, $V_{\text{eff}}(\xi)$, which is no longer a periodic function for a large probe-beam power and hence intensities along high-order diffraction directions disappear. However, $V_{\text{eff}}(\xi)$ is still $\mathcal{PT}$ symmetric but has a different ratio between the real and the imaginary parts in comparison with the linear potential $V(\xi)$ in Eq. (4). This implies that the nonlinear effect can change the domains of UPTP and BPTP, consistent with the result in Ref. [67]. If the probe beam is very wide ($w_0 \gg \Lambda$), $V_{\text{eff}}(\xi) \approx V(\xi) + 0.81$, i.e., there is only a constant difference between $V_{\text{eff}}(\xi)$ and $V(\xi)$, and $V_{\text{eff}}(\xi)$ becomes period again. In this case, the light diffraction will be the same as that in the linear case.

However, the nonlocality of the nonlocal Kerr nonlinearity contributed by the atom-atom interaction plays an important role in the nonlinear light diffraction from the EIG. To demonstrate this, the probe-beam propagation with a large nonlocality degree σ is numerically calculated, with the result shown in Fig. 5 for $\sigma = 10$. We see that, due to the large nonlocality degree of the Kerr nonlinearity, intensities of the diffraction fringes along high-order diffraction directions suppressed by the Kerr nonlinearity are partially recovered [see Figs. 5(a)–5(c)]. In addition, due to the large σ, the value of $A_{\min}$ is decreased to 10^{-4}. Moreover, the domain of the UPTP is enlarged with the increase in σ [comparing Fig. 5(d) with Fig. 4(d)], which implies that the increase in the nonlocality degree of the self-defocusing Kerr nonlinearity can be used to suppress the $\mathcal{PT}$ symmetry breaking.

The effect of the nonlocality degree on the nonlinear light diffraction patterns can be understood as follows. Consider the case of a very large σ, by which the nonlinear response function W_2 in Eq. (4) can be approximated to be spatially independent, i.e., $W_2(\xi - \xi') = W_2(\xi = 0) \equiv W_{20}$. As a result, the nonlocal Kerr nonlinearity term in Eq. (4) reduces to the form PW_{20}, with $W_{20} > 0$ (self-defocusing Kerr nonlinearity). Thus, one obtains an effective optical potential

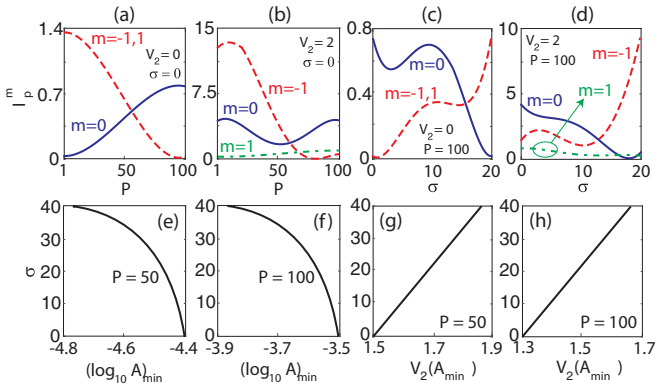

FIG. 6. (a–d) Intensities of nonlinear Raman-Nath diffraction fringes along the 0th- and ±1st-order diffraction directions (i.e., $I_p^{0,\pm1}$) as functions of the light power of the probe beam P and the nonlocality degree of the Kerr nonlinearity σ. $I_p^{0,\pm1}$ as a function of P for $V_2 = 0$ (a) and $V_2 = 2$ (b), with $\sigma = 0$; $I_p^{0,\pm1}$ as a function of σ for $V_2 = 0$ (c) and $V_2 = 2$ (d), with $P = 100$. σ as a function of the minimum of the logarithm of the symmetry degree A, $(\log_{10} A)_{\min}$, for $P = 50$ (e) and $P = 100$ (f); σ as a function of V_2 where $A_{\min}$ is achieved for $P = 50$ (g) and $P = 100$ (h).

$V_{\rm eff}(\xi) = V(\xi) + PW_{20}$, and hence the light diffraction in this case is similar to a linear one and the intensities along high-order diffraction directions are restored to that of a linear Raman-Nath diffraction.

It should be stressed that the Raman-Nath diffraction fringes illustrated above can be manipulated actively, which is useful for practical applications in the design of optical devices. Figures 6(a) and 6(b) show $I_p^{0,\pm1}$ (i.e., the intensities of the diffraction along the0th- and ±1st-order diffraction directions) as functions of the probe-beam power P for $V_2 = 0$ [Fig. 6(a)] and $V_2 = 2$ [Fig. 6(b)], respectively, with the nonlocality degree of the Kerr nonlinearity $\sigma = 0$; $I_p^{0,\pm1}$ are shown as functions of σ for $V_2 = 0$ [Fig. 6(c)] and $V_2 = 2$ [Fig. 6(d)], respectively, with probe-beam light power $P = 100$. In the figure we see that the intensities of the 0th-order and ±1st-order diffraction fringes can be adjusted by changing the incident power of the probe beam P and nonlocality degree of the Kerr nonlinearity σ. This property of the nonlinear Raman-Nath diffraction can be employed to realize optical beam dividers with desired intensities in different directions.

Moreover, by measuring the symmetry degree A of the nonlinear Raman-Nath diffraction fringes, it is possible to acquire the information of the nonlocality degree σ of the Kerr nonlinearity and, hence, to deduce values of the radius of the Rydberg-blockade sphere and the atomic dispersion coefficient. To demonstrate this, Fig. 6(e) [Fig. 6(f)] shows the result of σ as a function of the minimum of $\log_{10} A$, $(\log_{10} A)_{\min}$, for $P = 50$ [$P = 100$], and Fig. 6(g) [Fig. 6(h)] shows the result of σ as a function of $V_2(A_{\min})$ for $P = 50$ [$P = 100$]. We see that, by measuring either $(\log_{10} A)_{\min}$ or $V(A_{\min})$, the value of σ can be obtained. Then, by using the relations

$$R_b = \sigma w_0 \quad \text{and} \quad |C_6| = (\sigma w_0)^6 |\delta_{\rm EIT}|, \tag{14}$$

where $\delta_{\rm EIT}$ is the line width of the EIT transmission spectrum (i.e., the width of the EIT transparency window [66]), one can get the values of the radius of the Rydberg-blockade sphere R_b and the dispersion coefficient C_6 at the same time. Therefore, the intensity distribution of the nonlinear Raman-Nath diffraction fringes can indeed be used to characterize the interatomic interaction in Rydberg gases.

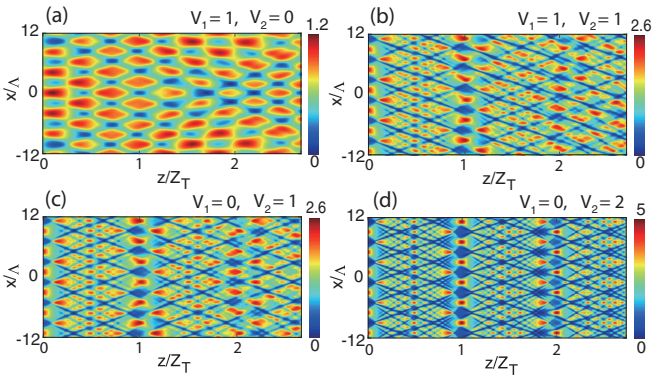

FIG. 7. Talbot diffraction patterns (self-imaging recurrences) in the Rydberg gas for different coefficients V_1 and V_2 of the $\mathcal{PT}$-symmetric EIG with $\sigma = 0$. The input condition is given in the text. (a–d) Probe-beam intensity $|U|^2$ as a function of x/Λ and z/Z_T for $(V_1, V_2) = (1, 0)$ (a), $(V_1, V_2) = (1, 1)$ (b), $(V_1, V_2) = (0, 1)$ (c), and $(V_1, V_2) = (0, 2)$ (d). The Talbot distance $Z_T \approx 2$ mm in all panels.

IV. TALBOT EFFECT BY $\mathcal{PT}$-SYMMETRIC EIGs

Now we turn to investigate a near-field nonlinear diffraction of the probe beam in the system. Particularly, we focus on the emergence of the Talbot effect, in which the self-imaging from the EIG illuminated by the probe beam can periodically replicate at certain imaging planes (more details are given in Appendix C). These imaging planes are located at even integer multiples of the so-called Talbot distance $Z_T = 2\Lambda^2/\lambda_p$ (where Λ is the spatial period of the EIG and λ_p the wavelength of the probe field; see Sec. III A). A possible setup for observing nonlinear Talbot carpets is shown in Fig. 1(c), where the $\mathcal{PT}$-symmetric EIG is created only in the left part of the atomic cell.

We first consider how the gain-absorption coefficient V_2 of the $\mathcal{PT}$-symmetric EIG influences Talbot self-imaging recurrences. Shown in Fig. 7 is the numerical result of a simulation of the Talbot diffraction effect in the Rydberg gas, with the probe-beam intensity $|U|^2$ taken to be a function of x/Λ and z/Z_T for $\sigma = 0$ and for different gain-absorption coefficients V_1 and V_2 of the $\mathcal{PT}$-symmetric EIG. Parameters are $(V_1, V_2) = (1, 0)$ [Fig. 7(a)], $(V_1, V_2) = (1, 1)$ [Fig. 7(b)], $(V_1, V_2) = (0, 1)$ [Fig. 7(c)], and $(V_1, V_2) = (0, 2)$ [Fig. 7(d)]. In the simulation, the Talbot distance $Z_T \approx 2$ mm, the input beam $U_{\rm in}(x) = U_0\, e^{-x^2/(2w_0^2)}$, with $U_0 = 0.12$, the beam radius $w_0 = 10\Lambda \approx 280\ \mu$m, and the light power $P \approx 1$.

In Fig. 7(a), we see that for $(V_1, V_2) = (1, 0)$ the Talbot pattern is not yet developed; but for $(V_1, V_2) = (1, 1)$ it forms quite well, which is shown in Fig. 7(b). Thus we conclude that the Talbot effect is mainly caused by the gain-absorption coefficient of the $\mathcal{PT}$-symmetric EIG, i.e., by nonzero V_2. To confirm this deduction, we carry out a further simulation with vanishing real part of the potential describing the $\mathcal{PT}$-symmetric EIG (i.e., $V_1 = 0$). Shown in Figs. 7(c) and

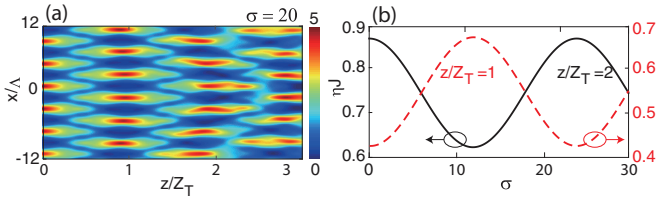

FIG. 8. Nonlinear Talbot diffraction patterns (self-imaging recurrences) in the Rydberg gas. The input condition is given in the text. (a) Probe-beam intensity $|U|^2$ as a function of x/Λ and z/Z_T for $\sigma = 20$. (b) Fidelity of the Talbot effect, characterized by the quantity ηJ (see text) as a function of σ at $z/Z_T = 1$ (dashed red line) and $z/Z_T = 2$ (solid black line).

7(d) are the Talbot patterns with $(V_1, V_2) = (0, 1)$ and (0,2), respectively. We see that the Talbot effect becomes more clear when $V_1 = 0$ and V_2 becomes larger. On the other hand, Z_T does not change in Figs. 7(c) and 7(d), indicating that the Talbot distance does not depend on V_2.

To see the influence of the Kerr nonlinearity on the Talbot effect, we can increase the incident intensity of the probe beam. We found, however, that the light power of the input beam P has a marginal effect on the Talbot self-imaging recurrences, i.e., the Talbot diffraction carpet obtained in the case has no significant difference from that shown in Fig. 7. This is because the input beam is a very wide Gaussian one, which can be approximated as a plane wave, and hence the Kerr nonlinearity provided by the Rydberg gas contributes only a constant phase to the probe beam.

However, the nonlocality degree σ of the nonlocal Kerr nonlinearity of the system has a drastic effect on the Talbot self-imaging recurrences. Figure 8(a) shows the result of a simulation of the Talbot effect by taking $|U|^2$ as a function of x/Λ and z/Z_T for $\sigma = 20$. The initial condition is the same as that used in Fig. 7, but with $U_0 = 1.2$ (and hence $P = 100$) and $(V_1, V_2) = (0, 2)$. In the figure we see that the Talbot intensity carpet disappears as σ increases.

The dashed red (solid black) line in Fig. 8(b) is the fidelity of the Talbot effect characterized by the quantity ηJ, which is taken as a function of σ for $z/Z_T = 1$ ($z/Z_T = 2$). Here, $\eta(z) \equiv \int_{-\infty}^{\infty} dx|U(x,z)|^2 / \int_{-\infty}^{\infty} dx|U_{\rm in}(x)|^2$ is the power ratio between the value at distance z and that at the input ($z = 0$), and $J(z)$ is the overlap integration

$$J(z) = \frac{|\int_{-\infty}^{\infty} dx U(x,z) U_{\rm in}(x)|^2}{\int_{-\infty}^{\infty} dx|U(x,z)|^2 \int_{-\infty}^{\infty} dx|U_{\rm in}(x)|^2}. \quad (15)$$

We see that the fidelities at $z/Z_T = 1$ and $z/Z_T = 2$ are both periodic functions of σ; furthermore, the maximum position of the fidelity for $z/Z_T = 2$ on the σ axis is the same as the minimum position of the fidelity for $z/Z_T = 1$, and vice versa. The physical reason is that the image at odd-integer multiples of the Talbot distance has half a period lateral shift with respect to the one at $z = 0$, while the image at even-integer multiples of the Talbot distance duplicates the one at $z = 0$. Obviously, the measurement of the fidelities for $z/Z_T = 1$ and 2 allows us to attain the value of the nonlocality degree σ and, hence, values of the Rydberg-blockade radius R_b and the dispersion parameter C_6 of the Rydberg atoms.

V. SUMMARY

In this work, we have proposed a scheme to realize EIGs with $\mathcal{PT}$ symmetry and investigated nonlinear light diffractions by $\mathcal{PT}$-symmetric EIGs in a cold Rydberg gas working under the condition of EIT. We have demonstrated that, for a far-field diffraction, probe laser beams incident upon the $\mathcal{PT}$-symmetric EIGs display distinctive asymmetric diffraction fringes, which can be actively manipulated through tuning the gain-absorption coefficient of the EIGs, the incident intensity of the probe beams, and the nonlocality degree of the Kerr nonlinearity contributed by the atom-atom interaction in the Rydberg gas. We have also demonstrated that, for a near-field diffraction, nonlinear Talbot diffraction carpets emerge, which can be modulated by the nonlocal Kerr nonlinearity, allowing us to realize controllable optical self-imaging. The results reported here are not only helpful for developing non-Hermitian nonlinear optics, but also promising for characterizing the atom-atom interaction in Rydberg gases and for designing new optical devices useful in optical information processing and transmission.

ACKNOWLEDGMENTS

This work was supported by the National Natural Science Foundation of China (NSFC) under Grants No. 11474099, No. 11475063, No. 11974117, and No. 11975098, National Key Research and Development Program of China under Grants No. 2017YFA0304201 and No. 2016YFA0302103, Program of Shanghai Academic Research Leader under Grant No. 17XD1401500, Engineering and Physical Sciences Research Council (EPSRC) under Grants No. EP/M014266/1 and No. EP/R04340X/1, and UKIERI-UGC Thematic Partnership under Grant No. IND/CONT/G/16-17/73.

APPENDIX A: BLOCH EQUATIONS OF DENSITY MATRIX ELEMENTS AND EXPRESSION OF THE NONLOCAL KERR NONLINEARITY

From the Hamiltonian given in the text, we obtain the optical Bloch equations of the density matrix elements, $\rho_{jl} \equiv \langle \hat{S}_{jl} \rangle$, with the form

$$i\frac{\partial}{\partial t}\rho_{11} + i\Gamma_{21}\rho_{11} - i\Gamma_{13}\rho_{33} - \Omega_p\rho_{13} + \Omega_p^*\rho_{31} = 0, \quad (A1a)$$

$$i\frac{\partial}{\partial t}\rho_{22} - i\Gamma_{21}\rho_{11} - i\Gamma_{23}\rho_{33} - \Omega_c\rho_{23} + \Omega_c^*\rho_{32} = 0, \quad (A1b)$$

$$i\frac{\partial}{\partial t}\rho_{33} + i\Gamma_{3}\rho_{33} - i\Gamma_{34}\rho_{44} + \Omega_p\rho_{13} - \Omega_p^*\rho_{31} + \Omega_c\rho_{23} - \Omega_c^*\rho_{32} - \Omega_a\rho_{34} + \Omega_a^*\rho_{43} = 0, \quad (A1c)$$

$$i\frac{\partial}{\partial t}\rho_{44}+i\Gamma_{34}\rho_{44}+\Omega_a\rho_{34}-\Omega_a^*\rho_{43}=0, \tag{A1d}$$

$$\left(i\frac{\partial}{\partial t}+d_{21}\right)\rho_{21}+\Omega_c^*\rho_{31}-\Omega_p\rho_{23}=0, \tag{A1e}$$

$$\left(i\frac{\partial}{\partial t}+d_{31}\right)\rho_{31}+\Omega_p(\rho_{11}-\rho_{33})+\Omega_c\rho_{21}+\Omega_a^*\rho_{41}=0, \tag{A1f}$$

$$\left(i\frac{\partial}{\partial t}+d_{41}\right)\rho_{41}+\Omega_a\rho_{31}-\Omega_p\rho_{43}-\mathcal{N}_\alpha\int d^3\mathbf{r}'V(\mathbf{r}'-\mathbf{r})\rho_{44,41}(\mathbf{r}',\mathbf{r},t)=0, \tag{A1g}$$

$$\left(i\frac{\partial}{\partial t}+d_{32}\right)\rho_{32}+\Omega_p\rho_{12}+\Omega_c(\rho_{22}-\rho_{33})+\Omega_a^*\rho_{42}=0, \tag{A1h}$$

$$\left(i\frac{\partial}{\partial t}+d_{42}\right)\rho_{42}+\Omega_a\rho_{32}-\Omega_c\rho_{43}-\mathcal{N}_\alpha\int d^3\mathbf{r}'V(\mathbf{r}'-\mathbf{r})\rho_{44,42}(\mathbf{r}',\mathbf{r},t)=0, \tag{A1i}$$

$$\left(i\frac{\partial}{\partial t}+d_{43}\right)\rho_{43}+\Omega_a(\rho_{33}-\rho_{44})-\Omega_p^*\rho_{41}-\Omega_c^*\rho_{42}-\mathcal{N}_\alpha\int d^3\mathbf{r}'V(\mathbf{r}'-\mathbf{r})\rho_{44,43}(\mathbf{r}',\mathbf{r},t)=0, \tag{A1j}$$

where $d_{jl}=\Delta_j-\Delta_l+i\gamma_{jl}$, with $\gamma_{ij}=(\Gamma_i+\Gamma_j)/2+\gamma_{ij}^{\rm col}$. Here $\Gamma_j=\sum_{i<j}\Gamma_{ij}$, with Γ_{ij} the spontaneous emission decay rate and $\gamma_{ij}^{\rm col}$ the dephasing rate from $|j\rangle$ to $|i\rangle$. In Eqs. (A1g), (A1i), and (A1j), we have used the notation $\rho_{jl,\mu\nu}(\mathbf{r}',\mathbf{r},t)\equiv\langle\hat{S}_{jl}(\mathbf{r}',t)\hat{S}_{\mu\nu}(\mathbf{r},t)\rangle$. Note that we assume all the atoms are initially populated in state $|1\rangle$, and hence the average of the operator $\hat{O}$ means $\langle\hat{O}\rangle=\langle G|\hat{O}|G\rangle$, with $|G\rangle=|1,1,1,\ldots,1\rangle$.

Since the system satisfies the parameter condition $(\Delta_3+\Delta_4)/\Omega_a\sim 10\gg 1$, the atomic population in Rydberg state $|4\rangle$ is very small and can be approximated to be 0. Thus, at zeroth ($m=0$) order, we obtain equations for $\rho_{11}^{(0)}$, $\rho_{22}^{(0)}$, and $\rho_{33}^{(0)}$, reading

$$\begin{pmatrix}-\Gamma_{21}&0&\Gamma_{13}\\ \Gamma_{21}&0&\Gamma_{23}\\ 1&1&1\end{pmatrix}\begin{pmatrix}\rho_{11}^{(0)}\\ \rho_{22}^{(0)}\\ \rho_{33}^{(0)}\end{pmatrix}=\begin{pmatrix}0\\ 2\,\mathrm{Im}\left(\Omega_a^*\rho_{32}^{(0)}\right)\\ 1\end{pmatrix}. \tag{A2}$$

In order to solve $\rho_{32}^{(0)}$, we also need equations for $\rho_{32}^{(0)}$, $\rho_{42}^{(0)}$, and $\rho_{43}^{(0)}$, which are given by

$$\begin{pmatrix}d_{32}&\Omega_c^*&0\\ \Omega_c&d_{42}&-\Omega_a\\ 0&-\Omega_a^*&d_{43}\end{pmatrix}\begin{pmatrix}\rho_{32}^{(0)}\\ \rho_{42}^{(0)}\\ \rho_{43}^{(0)}\end{pmatrix}=\begin{pmatrix}\Omega_a\left(\rho_{33}^{(0)}-\rho_{22}^{(0)}\right)\\ 0\\ -\Omega_c\rho_{33}^{(0)}\end{pmatrix}. \tag{A3}$$

The solutions of Eqs. (1), (A2), and (A3) read

$$\rho_{11}^{(0)}=-\Gamma_{13}X/[\Gamma_{21}\Gamma_{13}-(\Gamma_{21}+\Gamma_{13})X+\Gamma_{21}(\Gamma_{23}+Y)], \tag{A4a}$$

$$\rho_{22}^{(0)}=\Gamma_{21}(\Gamma_{13}+\Gamma_{23}+Y)/[\Gamma_{21}\Gamma_{13}-(\Gamma_{21}+\Gamma_{13})X+\Gamma_{21}(\Gamma_{23}+Y)], \tag{A4b}$$

$$\rho_{33}^{(0)}=-\Gamma_{21}X/[\Gamma_{21}\Gamma_{13}-(\Gamma_{21}+\Gamma_{13})X+\Gamma_{21}(\Gamma_{23}+Y)], \tag{A4c}$$

$$\rho_{32}^{(0)}=\left[-(d_{42}d_{43}-|\Omega_c|^2)\rho_{22}^{(0)}+(d_{42}d_{43}-|\Omega_c|^2+|\Omega_a|^2)\rho_{33}^{(0)}\right]\Omega_c/Z, \tag{A4d}$$

$$\rho_{42}^{(0)}=\left[d_{43}\rho_{22}^{(0)}-(d_{32}+d_{43})\rho_{33}^{(0)}\right]\Omega_c\Omega_a/Z, \tag{A4e}$$

$$\rho_{43}^{(0)}=\left[|\Omega_c|^2\rho_{22}^{(0)}-(d_{32}d_{42}+|\Omega_c|^2-|\Omega_a|^2)\rho_{33}^{(0)}\right]\Omega_a/Z, \tag{A4f}$$

$$\rho_{21}^{(0)}=\rho_{31}^{(0)}=\rho_{41}^{(0)}=\rho_{44}^{(0)}=0, \tag{A4g}$$

where $X=2\,\mathrm{Im}[(d_{42}d_{43}-|\Omega_c|^2)|\Omega_c|^2/Z]$ and $Y=-2\,\mathrm{Im}[(d_{42}d_{43}-|\Omega_c|^2+|\Omega_a|^2)|\Omega_c|^2/Z]$, with $Z=d_{32}d_{42}d_{43}-|\Omega_c|^2d_{32}-|\Omega_a|^2d_{43}$.

At first ($m=1$) order, the solution for nonzero matrix elements reads $\rho_{21}^{(1)}=\alpha_{21}^{(1)}\Omega_p$, $\rho_{31}^{(1)}=\alpha_{31}^{(1)}\Omega_p$, $\rho_{41}^{(1)}=\alpha_{41}^{(1)}\Omega_p$, where $\alpha_{21}^{(1)}$, $\alpha_{31}^{(1)}$, $\alpha_{41}^{(1)}$ are determined by the equation

$$\begin{pmatrix}d_{21}&\Omega_a^*&0\\ \Omega_a&d_{31}&\Omega_c^*\\ 0&\Omega_c&d_{41}\end{pmatrix}\begin{pmatrix}\alpha_{21}^{(1)}\\ \alpha_{31}^{(1)}\\ \alpha_{41}^{(1)}\end{pmatrix}=\begin{pmatrix}\rho_{23}^{(0)}\\ \rho_{33}^{(0)}-\rho_{11}^{(0)}\\ \rho_{43}^{(0)}\end{pmatrix}. \tag{A5}$$

Expressions of $\alpha_{21}^{(1)}$, $\alpha_{31}^{(1)}$, and $\alpha_{41}^{(1)}$ are obtained from Eq. (A5), reading

$$\alpha_{21}^{(1)} = \left[(d_{31}d_{41} - |\Omega_a|^2)\rho_{23}^{(0)} + \Omega_c^*\Omega_a^*\rho_{43}^{(0)} - d_{41}\Omega_c^*\left(\rho_{33}^{(0)} - \rho_{11}^{(0)}\right)\right]/D, \tag{A6a}$$

$$\alpha_{31}^{(1)} = \left[d_{21}d_{41}\left(\rho_{33}^{(0)} - \rho_{11}^{(0)}\right) - d_{41}\Omega_c\rho_{23}^{(0)} - d_{21}\Omega_a^*\rho_{43}^{(0)}\right]/D, \tag{A6b}$$

$$\alpha_{41}^{(1)} = \left[(d_{21}d_{31} - |\Omega_c|^2)\rho_{43}^{(0)} + \Omega_c\Omega_a\rho_{23}^{(0)} - d_{21}\Omega_a\left(\rho_{33}^{(0)} - \rho_{11}^{(0)}\right)\right]/D, \tag{A6c}$$

where $D = d_{21}d_{31}d_{41} - |\Omega_c|^2 d_{41} - |\Omega_a|^2 d_{21}$.

At second ($m = 2$) order, the solution for nonzero matrix elements is found to be $\rho_{32}^{(2)} = \alpha_{32}^{(2)}|\Omega_p|^2$, $\rho_{42}^{(2)} = \alpha_{42}^{(2)}|\Omega_p|^2$, $\rho_{43}^{(2)} = \alpha_{43}^{(2)}|\Omega_p|^2$, $\rho_{jj}^{(2)} = \alpha_{jj}^{(2)}|\Omega_p|^2$ ($j = 1, 2, 3, 4$), with $\alpha_{32}^{(2)}$, $\alpha_{42}^{(2)}$, $\alpha_{43}^{(2)}$ satisfying the equation

$$\begin{pmatrix} d_{32} & \Omega_c^* & 0 \\ \Omega_c & d_{42} & -\Omega_a \\ 0 & -\Omega_2^* & d_{43} \end{pmatrix}\begin{pmatrix} \alpha_{32}^{(2)} \\ \alpha_{42}^{(2)} \\ \alpha_{43}^{(2)} \end{pmatrix} - \begin{pmatrix} \Omega_a(\alpha_{33}^{(2)} - \alpha_{22}^{(2)}) - \alpha_{12}^{(1)} \\ 0 \\ \Omega_c(\alpha_{44}^{(2)} - \alpha_{33}^{(2)}) + \alpha_{41}^{(1)} \end{pmatrix} \tag{A7}$$

and $\alpha_{jj}^{(2)}$ satisfying the equation

$$\begin{pmatrix} -\Gamma_{21} & 0 & \Gamma_{13} & 0 \\ \Gamma_{21} & 0 & \Gamma_{23} & 0 \\ 0 & 0 & -\Gamma_{13} - \Gamma_{23} & \Gamma_{34} \\ 1 & 1 & 1 & 1 \end{pmatrix}\begin{pmatrix} \alpha_{11}^{(2)} \\ \alpha_{22}^{(2)} \\ \alpha_{33}^{(2)} \\ \alpha_{44}^{(2)} \end{pmatrix} - \begin{pmatrix} 2\,\mathrm{Im}\left(\alpha_{31}^{(1)}\right) \\ 2\,\mathrm{Im}\left(\Omega_a^*\alpha_{32}^{(2)}\right) \\ 2\,\mathrm{Im}\left(\alpha_{31}^{(1)*} + \Omega_a\alpha_{32}^{(2)*} + \Omega_c^*\alpha_{43}^{(2)}\right) \\ 0 \end{pmatrix}. \tag{A8}$$

Expressions for $\alpha_{32}^{(2)}$, $\alpha_{42}^{(2)}$, $\alpha_{43}^{(2)}$, and $\alpha_{jj}^{(2)}$ ($j = 1$, 2, 3, and 4) are obtained from Eqs. (A7) and (A8). However, they are too lengthy to be presented here and are treated by numerical means.

The expression of the nonlocal Kerr nonlinearity is obtained at third ($m = 3$) order. The solution of $\rho_{j1}^{(3)}$ ($j = 1$, 2, and 3) can be obtained from the equation

$$\begin{pmatrix} d_{21} & \Omega_a^* & 0 \\ \Omega_a & d_{31} & \Omega_c^* \\ 0 & \Omega_c & d_{41} \end{pmatrix}\begin{pmatrix} \rho_{21}^{(3)} \\ \rho_{31}^{(3)} \\ \rho_{41}^{(3)} \end{pmatrix} = \begin{pmatrix} \alpha_{23}^{(2)} \\ \alpha_{33}^{(2)} - \alpha_{11}^{(2)} \\ \alpha_{43}^{(2)} \end{pmatrix}|\Omega_p|^2\Omega_p + \begin{pmatrix} 0 \\ 0 \\ \mathcal{N}_\alpha \int \mathbf{r}' V(\mathbf{r}' - \mathbf{r})\alpha_{41}^{(1)*}\alpha_{4141}^{(2)}|\Omega_p(\mathbf{r}')|^2\Omega_p(\mathbf{r}) \end{pmatrix}, \tag{A9}$$

where $\alpha_{4141}^{(2)}$ can be obtained from the equation

$$\begin{pmatrix} d_{21} & 0 & 0 & \Omega_a^* & 0 & 0 \\ 0 & d_{31} & 0 & \Omega_a & 0 & \Omega_c^* \\ 0 & 0 & d_{41} - V/2 & 0 & 0 & \Omega_c \\ \Omega_a & \Omega_a^* & 0 & d_{21} + d_{31} & \Omega_c^* & 0 \\ 0 & 0 & 0 & \Omega_c & d_{21} + d_{41} & \Omega_a^* \\ 0 & \Omega_c & \Omega_c^* & 0 & \Omega_a & d_{31} + d_{41} \end{pmatrix}\begin{pmatrix} \alpha_{2121}^{(2)} \\ \alpha_{3131}^{(2)} \\ \alpha_{4141}^{(2)} \\ \alpha_{2131}^{(2)} \\ \alpha_{2141}^{(2)} \\ \alpha_{3141}^{(2)} \end{pmatrix} = \begin{pmatrix} \rho_{23}^{(0)}\alpha_{21}^{(1)} \\ \left(\rho_{33}^{(0)} - \rho_{11}^{(0)}\right)\alpha_{31}^{(1)} \\ \rho_{43}^{(0)}\alpha_{41}^{(1)} \\ \left(\rho_{33}^{(0)} - \rho_{11}^{(0)}\right)\alpha_{21}^{(1)} + \rho_{23}^{(0)}\alpha_{31}^{(1)} \\ \rho_{23}^{(0)}\alpha_{41}^{(1)} + \rho_{43}^{(0)}\alpha_{21}^{(1)} \\ \left(\rho_{33}^{(0)} - \rho_{11}^{(0)}\right)\alpha_{41}^{(1)} + \rho_{43}^{(0)}\alpha_{31}^{(1)} \end{pmatrix}. \tag{A10}$$

Expressions for $\alpha_{21}^{(3)}$, $\alpha_{31}^{(3)}$, $\alpha_{41}^{(3)}$, $\alpha_{j1j1}^{(2)}$ ($j = 2$, 3, and 4), $\alpha_{2131}^{(2)}$, $\alpha_{2141}^{(2)}$, and $\alpha_{3141}^{(2)}$ are obtained from Eqs. (A9) and (A10). However, they are too lengthy to be presented here and are treated by numerical means. With expressions for $\alpha_{31}^{(1)}$, $\alpha_{11}^{(2)}$, $\alpha_{33}^{(2)}$, $\alpha_{23}^{(2)}$, $\alpha_{43}^{(2)}$, $\alpha_{41}^{(1)}$, and $\alpha_{4141}^{(2)}$ at hand, we can obtain the expressions for $\chi_p^{(1)}$, $\chi_{p,1}^{(3)}$, and $\chi_{p,2}^{(3)}(\mathbf{r}' - \mathbf{r})$.

APPENDIX B: DESIGN OF THE SPATIALLY MODULATED CONTROL AND ASSISTED FIELDS

The method for engineering the spatially modulated control and assisted fields is given in the following. First, we note that the optical potential with $\mathcal{PT}$ symmetry must be real at the origin $\xi = 0$, i.e., $V_i(\xi = 0) = 0$. To get a $\mathcal{PT}$-symmetric potential that has balanced gain and loss in the whole space, we assume that the Rabi frequencies of the control and assisted field are space dependent, $\Omega_c = \Omega_c(\xi)$ and $\Omega_a = \Omega_a(\xi)$. Thus if $\Omega_c = \Omega_{c0}$ and $\Omega_a = \Omega_{a0}$ at $\xi = 0$, the value of Δ_3 can be determined by solving the equation $V_i(\Omega_{c0}, \Omega_{a0}, \Delta_3) = 0$, referred to as $\Delta_3 = \Delta_{30}$, and hence the values of Δ_2 and Δ_4 can also be determined.

Next, we expand V_r and V_i around $\Omega_c = \Omega_{c0}$ and $\Omega_a = \Omega_{a0}$, i.e.,

$$V_r(\Omega_c, \Omega_a, \Delta_{30}) = V_r(\Omega_{c0}, \Omega_{a0}, \Delta_{30}) + R_{1,0}(\Omega_c - \Omega_{c0}) + R_{0,1}(\Omega_a - \Omega_{a0}), \tag{B1a}$$

$$V_i(\Omega_c, \Omega_a, \Delta_{30}) = I_{1,0}(\Omega_c - \Omega_{c0}) + I_{0,1}(\Omega_a - \Omega_{a0}), \tag{B1b}$$

where

$$R_{m,n} = \frac{\partial^{m+n}}{\partial^m \Omega_c \partial^n \Omega_a} V_r(\Omega_c, \Omega_a, \Delta_{30})|_{\Omega_c=\Omega_{c0},\Omega_a=\Omega_{a0}},$$
$$I_{m,n} = \frac{\partial^{m+n}}{\partial^m \Omega_c \partial^n \Omega_a} V_i(\Omega_c, \Omega_a, \Delta_{30})|_{\Omega_c=\Omega_{c0},\Omega_a=\Omega_{a0}}. \quad \text{(B2)}$$

Note that we have truncated the expansions by neglecting high-order terms, which means that Ω_c and Ω_a are taken as weakly space dependent.

Finally, in order to determine the spatial distributions of $\Omega_c(\xi)$ and $\Omega_a(\xi)$, we solve the equations

$$R_{1,0}(\Omega_c - \Omega_{c0}) + R_{0,1}(\Omega_a - \Omega_{a0}) = V_{Tr}(\xi) - V_r(\Omega_{c0}, \Omega_{a0}, \Delta_{30}), \quad \text{(B3a)}$$
$$I_{1,0}(\Omega_c - \Omega_{c0}) + I_{0,1}(\Omega_a - \Omega_{a0}) = V_{Ti}(\xi), \quad \text{(B3b)}$$

where $V_T(\xi)$ denotes the target potential, which possesses $\mathcal{PT}$ symmetry. If $\Omega_c(\xi)$ and $\Omega_a(\xi)$ can be solved through Eq. (B3), the target $\mathcal{PT}$-symmetric potential will be obtained successfully.

Note that the potential engineering method described above provides an accurate $\mathcal{PT}$ symmetry only for small ξ. This imposes a constraint on the choice of the width of the probe beam, which should be small enough so that the undesirable deviation from the $\mathcal{PT}$ symmetry at large ξ can be avoided.

APPENDIX C: BASIC THEORY OF THE TALBOT EFFECT

According to the Fresnel-Kirchhoff diffraction theory [68], the diffracted field amplitude $E(\mathbf{R})$ is defined in terms of the amplitude transmission of the object $A(\mathbf{r})$ and the coherent amplitude of the source $S(\mathbf{r}_s)$. Here, $\mathbf{R}$, $\mathbf{r}$, and $\mathbf{r}_s$ are located at the observation, object, and source planes, respectively. In the paraxial approximation, $E(\mathbf{R})$ takes the form

$$E(\mathbf{R}) = \frac{\exp[2i\pi(d_1+d_2)/\lambda]}{i\lambda d_1 d_2} \int d\mathbf{r}_s S(\mathbf{r}_s) \int d\vec{r} A(\mathbf{r}) \times \exp\left[\frac{i\pi|\mathbf{r}-\mathbf{r}_s|^2}{\lambda d_1}\right] \exp\left[\frac{i\pi|\mathbf{R}-\mathbf{r}|^2}{\lambda d_2}\right], \quad \text{(C1)}$$

where d_1 is the propagation distance between the object and the source and d_2 is the distance from the object to the observation plane. For a plane-wave illumination, the diffraction amplitude $E(\mathbf{R})$ at a distance z from the object is proportional to

$$E(\mathbf{R}, z) \propto \int_{-\infty}^{\infty} d\mathbf{r} A(\mathbf{r}) e^{i\Phi(\mathbf{R},\mathbf{r},z)}, \quad \text{(C2)}$$

where $\Phi(\mathbf{R}, \mathbf{r}, z) \equiv \frac{2\pi}{\lambda}(z + \frac{\mathbf{R}^2}{2z} - \frac{\mathbf{r}\cdot\mathbf{R}}{z} + \frac{\mathbf{r}^2}{2z})$. The integration is performed over the infinite boundary on the object plane. Substituting

$$A(\mathbf{r}) = \sum_{n=-\infty}^{n=\infty} C_n \exp\left(i\frac{2\pi n|\mathbf{r}|}{d}\right) \quad \text{(C3)}$$

into Eq. (C2), we obtain

$$E(\mathbf{R}, z) \propto \sum_{n=-\infty}^{n=\infty} C_n \exp\left(-i\frac{\pi\lambda n^2 z}{d^2}\right) \exp\left(i\frac{2\pi n|\mathbf{R}|}{d}\right), \quad \text{(C4)}$$

where C_n is the amplitude of the nth harmonic. At a certain distance z, all diffraction orders are in phase and reinforced by satisfying the condition $z = m\Lambda^2/\lambda_p$, where m, a positive integer, is referred to as the self-imaging number. For $m = 1$, $z = \Lambda^2/\lambda_p \equiv z_T$ is the Talbot length. In planes of $z = mz_T$, the diffracted field can repeat the amplitude at the output plane of the grating with and without the shifted half-period $\Lambda/2$ for odd and even integers m, respectively.

In the text, we calculate the fidelity between the image at $z = mz_T$ and that at $z = 0$. We find that the fidelity reaches its maximum ($\approx$1) at even-integer multiples of the Talbot length, whereas it reaches its minimum ($\approx$0) at odd-integer multiples of the Talbot length.

[1] E. G. Loewen and E. Popov, *Diffraction Gratings and Applications (Optical Science and Engineering)*, 1st ed. (CRC Press, Boca Raton, FL, 1997).

[2] C. Palmer and E. G. Loewen, *Diffraction Grating Handbook* (Newport, Rochester, NY, 2005).

[3] H. Y. Ling, Y. Q. Li, and M. Xiao, Electromagnetically induced grating: Homogeneously broadened medium, Phys. Rev. A **57**, 1338 (1998).

[4] M. Mitsunaga and N. Imoto, Observation of an electromagnetically induced grating in cold sodium atoms, Phys. Rev. A **59**, 4773 (1999).

[5] G. C. Cardoso and J. W. R. Tabosa, Electromagnetically induced gratings in a degenerate open two-level system, Phys. Rev. A **65**, 033803 (2002).

[6] A. W. Brown and M. Xiao, All-optical switching and routing based on an electromagnetically induced absorption grating, Opt. Lett. **30**, 699 (2005).

[7] L. E. E. de Araujo, Electromagnetically induced phase grating, Opt. Lett. **35**, 977 (2010).

[8] S. A. Carvalho and L. E. E. de Araujo, Electromagnetically induced phase grating: A coupled-wave theory analysis, Opt. Express **19**, 1936 (2011).

[9] L. Zhao, W. Duan, and S. F. Yelin, All-optical beam control with high speed using image-induced blazed gratings in coherent media, Phys. Rev. A **82**, 013809 (2010).

[10] L. Zhao, W. Duan, and S. F. Yelin, Generation of tunable-volume transmission-holographic gratings at low light levels, Phys. Rev. A **84**, 033806 (2011).

[11] R. G. Wan, J. Kou, L. Jiang, Y. Jiang, and J. Y. Gao, Electromagnetically induced grating via enhanced nonlinear modulation by spontaneously generated coherence, Phys. Rev. A **83**, 033824 (2011).

[12] S. Q. Kuang, C. S. Jin, and C. Li, Gain-phase grating based on spatial modulation of active Raman gain in cold atoms, Phys. Rev. A **84**, 033831 (2011).

[13] L. Wang, F. Zhou, P. Hu, Y. Niu, and S. Gong, Two-dimensional electromagnetically induced cross-grating in a four-level tripod type atomic system, J. Phys. B **47**, 225501 (2014).

[14] V. G. Arkhipkin and S. A. Myslivets, One- and two-dimensional Raman-induced diffraction gratings in atomic media, Phys. Rev. A **98**, 013838 (2018).

[15] J. A. Porto, F. J. García-Vidal, and J. B. Pendry, Transmission Resonances on Metallic Gratings with Very Narrow Slits, Phys. Rev. Lett. **83**, 2845 (1999).

[16] D. Fattal, J. Li, Z. Peng, M. Fiorentino, and R. G. Beausoleil, Flat dielectric grating reflectors with focusing abilities, Nat. Photonics **4**, 466 (2010).

[17] K. Patorski, The self-imaging phenomenon and its applications, Prog. Opt. **27**, 1 (1989).

[18] Y. Zhang, J. Wen, S. N. Zhu, and M. Xiao, Nonlinear Talbot Effect, Phys. Rev. Lett. **104**, 183901 (2010).

[19] Z. Zhang, X. Liu, D. Zhang, J. Sheng, Y. Zhang, Y. Zhang, and M. Xiao, Observation of electromagnetically induced Talbot effect in an atomic system, Phys. Rev. A **97**, 013603 (2018).

[20] Y. Zhang, Z. Wang, Z. Nie, C. Li, H. Chen, K. Lu, and M. Xiao, Four-Wave Mixing Dipole Soliton in Laser-Induced Atomic Gratings, Phys. Rev. Lett. **106**, 093904 (2011).

[21] Y. Zhang, Z. Wu, M. R. Belic, H. Zheng, Z. Wang, M. Xiao, and Y. Zhang, Photonic Floquet topological insulators in atomic ensembles, Laser Photonics Rev. **9**, 331 (2015).

[22] C. Hang, G. Huang, and V. V. Konotop, $\mathcal{PT}$ Symmetry with a System of Three-Level Atoms, Phys. Rev. Lett. **110**, 083604 (2013).

[23] J. Sheng, M. Miri, D. N. Christodoulides, and M. Xiao, $\mathcal{PT}$-symmetric optical potentials in a coherent atomic medium, Phys. Rev. A **88**, 041803(R) (2013).

[24] Z. Zhang, Y. Zhang, J. Sheng, L. Yang, M. Miri, D. N. Christodoulides, B. He, Y. Zhang, and M. Xiao, Observation of Parity-Time Symmetry in Optically Induced Atomic Lattices, Phys. Rev. Lett. **117**, 123601 (2016).

[25] Ziauddin, Y.-L. Chuang, and R.-K. Lee, $\mathcal{PT}$-symmetry in Rydberg atoms, Europhys. Lett. **115**, 14005 (2016).

[26] C. Hang and G. Huang, Parity-time symmetry with coherent atomic gases, Adv. Phys. X **2**, 737 (2017).

[27] Z. Zhang, D. Ma, J. Sheng, Y. Zhang, Y. Zhang, and M. Xiao, Non-Hermitian optics in atomic systems, J. Phys. B **51**, 072001 (2018).

[28] S. Boettcher and C. M. Bender, Real Spectra in Non-Hermitian Hamiltonians Having PT Symmetry, Phys. Rev. Lett. **80**, 5243 (1998).

[29] C. M. Bender, Making sense of non-Hermitian Hamiltonians, Rep. Prog. Phys. **70**, 947 (2007).

[30] V. V. Konotop, J. Yang, and D. A. Zezyulin, Nonlinear waves in $\mathcal{PT}$-symmetric systems, Rev. Mod. Phys. **88**, 035002 (2016).

[31] R. El-Ganainy, K. G. Makris, M. Khajavikhan, Z. H. Musslimani, S. Rotter, and D. N. Christodoulides, Non-Hermitian physics and $\mathcal{PT}$ symmetry, Nat. Phys. **14**, 11 (2018).

[32] L. Feng, R. El-Ganainy, and L. Ge, Non-Hermitian photonics based on parity-time symmetry, Nat. Photonics **11**, 752 (2017).

[33] H. Ramezani, T. Kottos, R. El-Ganainy, and D. N. Christodoulides, Unidirectional nonlinear $\mathcal{PT}$-symmetric optical structures, Phys. Rev. A **82**, 043803 (2010).

[34] L. Feng, M. Ayache, J. Huang, Y.-L. Xu, M.-H. Lu, Y.-F. Chen, Y. Fainman, and A. Scherer, Nonreciprocal light propagation in a silicon photonic circuit, Science **333**, 729 (2011).

[35] Z. Lin, H. Ramezani, T. Eichelkraut, T. Kottos, H. Cao, and D. Christodoulides, Unidirectional Invisibility Induced by $\mathcal{PT}$-Symmetric Periodic Structures, Phys. Rev. Lett. **106**, 213901 (2011).

[36] S. Longhi, $\mathcal{PT}$-symmetric laser absorber, Phys. Rev. A **82**, 031801(R) (2010).

[37] Y. D. Chong, L. Ge, and A. D. Stone, $\mathcal{PT}$-Symmetry Breaking and Laser-Absorber Modes in Optical Scattering Systems, Phys. Rev. Lett. **106**, 093902 (2011).

[38] Y. Sun, W. Tan, H. Li, J. Li, and H. Chen, Experimental Demonstration of a Coherent Perfect Absorber with $\mathcal{PT}$ Phase Transition, Phys. Rev. Lett. **112**, 143903 (2014).

[39] V. V. Konotop, V. S. Shchesnovich, and D. A. Zezyulin, Giant ampliffication of modes in parity-time symmetric waveguides, Phys. Lett. A **376**, 2750 (2012).

[40] L. Feng, Z. J. Wong, R. Ma, Y. Wang, and X. Zhang, Single mode laser by parity-time symmetry breaking, Science **346**, 972 (2014).

[41] H. Hodaei, M.-A. Miri, M. Heinrich, D. N. Christodoulides, and M. Khajavikhan, Parity-time-symmetric microring lasers, Science **346**, 975 (2014).

[42] H. Hodaei, A. U. Hassan, S. Wittek, H. Garcia-Gracia, R. El-Ganainy, D. N. Christodoulides, and M. Khajavikhan, Enhanced sensitivity at higher-order exceptional points, Nature **548**, 187 (2017).

[43] W. Chen, Ş. K. Özdemir, G. Zhao, J. Wiersig, and L. Yang, Exceptional points enhance sensing in an optical microcavity, Nature **548**, 192 (2017).

[44] L. Xiao, X. Zhan, Z. H. Bian, K. K. Wang, X. Zhang, X. P. Wang, J. Li, K. Mochizuki, D. Kim, N. Kawakami, W. Yi, H. Obuse, B. C. Sanders, and P. Xue, Observation of topological edge states in parity-time-symmetric quantum walks, Nat. Phys. **13**, 1117 (2017).

[45] Y. V. Kartashov, V. A. Vysloukh, V. V. Konotop, and L. Torner, Diffraction control in $\mathcal{PT}$-symmetric photonic lattices: From beam rectification to dynamic localization, Phys. Rev. A **93**, 013841 (2016).

[46] X.-Y. Zhu, Y.-L. Xu, Y. Zou, X.-C. Sun, C. He, M.-H. Lu, X.-P. Liu, and Y.-F. Chen, Asymmetric diffraction based on a passive parity-time grating, Appl. Phys. Lett. **109**, 111101 (2016).

[47] Y.-M. Liu, F. Gao, C.-H. Fan, and J.-H. Wu, Asymmetric light diffraction of an atomic grating with $\mathcal{PT}$ symmetry, Opt. Lett. **42**, 4283 (2017).

[48] T. Shui, W.-X. Yang, S. Liu, and L. Li, Asymmetric diffraction by atomic gratings with optical $\mathcal{PT}$ symmetry in the Raman-Nath regime, Phys. Rev. A **97**, 033819 (2018).

[49] D. Ma, D. Yu, X. Zhao, and J. Qian, Unidirectional and controllable higher-order diffraction by a Rydberg electromagnetically induced grating, Phys. Rev. A **99**, 033826 (2019).

[50] H. Ramezani, D. N. Christodoulides, V. Kovanis, I. Vitebskiy, and T. Kottos, $\mathcal{PT}$-Symmetric Talbot Effects, Phys. Rev. Lett. **109**, 033902 (2012).

[51] T. F. Gallagher, *Rydberg Atoms* (Cambridge University Press, Cambridge, UK, 2008).

[52] S. Sevincli, N. Henkel, C. Ates, and T. Pohl, Nonlocal Nonlinear Optics in Cold Rydberg Gases, Phys. Rev. Lett. **107**, 153001 (2011).

[53] J. D. Pritchard, K. J. Weatherill, and C. S. Adams, Nonlinear optics using cold Rydberg atoms, Annu. Rev. Cold At. Mol. **1**, 301 (2013).

[54] W. Li, D. Viscor, S. Hofferberth, and I. Lesanovsky, Electromagnetically Induced Transparency in an Entangled Medium, Phys. Rev. Lett. **112**, 243601 (2014).

[55] D. Viscor, W. Li, and I. Lesanovsky, Electromagnetically induced transparency of a single-photon in dipole-coupled one-dimensional atomic clouds, New J. Phys. **17**, 033007 (2015).

[56] Z. Bai, W. Li, and G. Huang, Stable single light bullets and vortices and their active control in cold Rydberg gases, Optica **6**, 309 (2019).

[57] O. Firstenberg, C. S. Adams, and S. Hofferberth, Nonlinear quantum optics mediated by Rydberg interactions, J. Phys. B **49**, 152003 (2016).

[58] C. Murray and T. Pohl, Quantum and nonlinear optics in strongly interacting atomic ensembles, *Advances in Atomic, Molecular, and Optical Physics* (Academic Press, New York, 2016), Vol. 65, pp. 321–372.

[59] M. Saffman, T. G. Walker, and K. Mølmer, Quantum information with Rydberg atoms, Rev. Mod. Phys. **82**, 2313 (2010).

[60] W. Li and I. Lesanovsky, Coherence in a cold-atom photon switch, Phys. Rev. A **92**, 043828 (2015).

[61] H. Gorniaczyk, C. Tresp, P. Bienias, A. Paris-Mandoki, W. Li, I. Mirgorodskiy, H. P. Büchler, I. Lesanovsky, and S. Hofferberth, Enhancement of Rydberg-mediated single-photon nonlinearities by electrically tuned Förster resonances, Nat. Commun. **7**, 12480 (2016).

[62] Y.-M. Liu, X.-D. Tian, X. Wang, D. Yan, and J.-H. Wu, Cooperative nonlinear grating sensitive to light intensity and photon correlation, Opt. Lett. **41**, 408 (2016).

[63] C. Hang and G. Huang, Parity-time symmetry along with nonlocal optical solitons and their active controls in a Rydberg atomic gas, Phys. Rev. A **98**, 043840 (2018).

[64] Z. Bai and G. Huang, Enhanced third-order and Fifth-order Kerr nonlinearities in a cold atomic system via Rydberg-Rydberg interaction, Opt. Express **24**, 4442 (2016).

[65] Q. Zhang, Z. Bai, and G. Huang, Fast-responding property of electromagnetically induced transparency in Rydberg atoms, Phys. Rev. A **97**, 043821 (2018).

[66] The radius of the blockade sphere, R_b, is estimated by $R_b = (|C_6/\delta_{\mathrm{EIT}}|)^{1/6}$, with δ_{EIT} the line width of the EIT transmission spectrum (i.e., the width of the EIT transparency window), calculated by $\delta_{\mathrm{EIT}} = |\Omega_c|^2/\gamma_{31}$ for $\Delta_3 = 0$ and $\delta_{\mathrm{EIT}} \approx |\Omega_c|^2/\Delta_3$ for $\Delta_3 \gg \gamma_{31}$.

[67] Y. Lumer, Y. Plotnik, M. C. Rechtsman, and M. Segev, Nonlinearly Induced $\mathcal{PT}$ Transition in Photonic Systems, Phys. Rev. Lett. **111**, 263901 (2013).

[68] M. Born and E. Wolf, *Principles of Optics*, 7th (expanded) ed. (Cambridge University Press, Cambridge, UK, 1999).